Nano-Micro Letters

e-ISSN 2150-5551
CN 31-2103/TB

ARTICLE

https://doi.org/10.1007/s40820-026-02172-1

Cite as
Nano-Micro Lett.
(2026) 18:333

Received: 23 December 2025
Accepted: 8 March 2026

Integrating Overall Water Splitting with Advanced Oxidation for Wastewater Treatment Using a Bifunctional Medium-Entropy Amorphous Alloy

Yifan Cui[1,2,3,4], Yonghui Wang[5], Bo Li[1,4], Jiaqi Huang[1,4], Le Bo[1,4], Hengqi Liu[5], Mahlanyane Kenneth Mathe[6], Murodjon Samadiy[7], Shengfeng Guo[8], Hongxian Shen[1,4], Jianfei Sun[1,4], Sida Jiang[1,2,3,4] ✉

HIGHLIGHTS

- $(FeCoNi)_{80}B_{20}$ fibers were prepared via a melt-extraction method with a high cooling rate to construct a crystalline–amorphous heterostructure. A substantial quantity of fibers (~ 100 g) was produced in a single batch, resulting in a competitive cost of approximately 0.51 USD per gram with accurate composition and high quality.
- In simulated reclaimed water, complete decolorization of the solution was achieved within 60 min, whereas the water splitting process maintained stable operation for approximately 115 h. The total organic carbon removal rate reached 63.24%.

ABSTRACT Hydrogen energy is regarded as a clean and reliable approach for storing intermittent energy sources. However, stringent water quality requirements remain critical challenges. The development of a bifunctional catalyst capable of simultaneously driving overall water splitting and degrading pollutants in wastewater can substantially enhance energy utilization efficiency and enable resource recycling. Nevertheless, the mismatch in the optimal pH conditions and the difficulty in balancing degradation efficiency and electrolysis performance remain notable obstacles. In this study, $(FeCoNi)_{80}B_{20}$ medium-entropy amorphous alloy (MEAA) fibers were prepared using a low-cost melt-extraction method. Owing to the crystalline–amorphous heterostructure, the fibers achieved complete decolorization within 90 s, while remaining effective across a wide pH range. In addition, the $(FeCoNi)_{80}B_{20}$ delivered overpotentials of 275 and 220 mV for the oxygen evolution reaction and hydrogen evolution reaction, respectively. By synchronizing both catalytic reactions, the $(FeCoNi)_{80}B_{20}$ enabled direct water splitting in reclaimed water, achieving complete decolorization while preserving electrocatalytic stability in an anion-exchange-membrane electrolyzer for 100 h under highly alkaline conditions (pH = 13.6). Moderate OH* adsorption endowed $(FeCoNi)_{80}B_{20}$ with excellent ability. This bifunctional catalyst addresses the coupled challenges of energy storage and water scarcity and offers a promising foundation for industrial implementation.

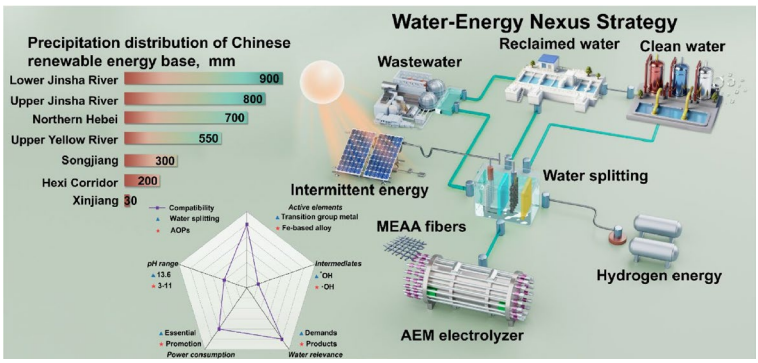

KEYWORDS Medium-entropy amorphous alloy; Crystalline-amorphous heterostructure; Water splitting; Water remediation; Water–energy nexus strategy

✉ Sida Jiang, jiangsida@hit.edu.cn
[1] School of Materials Science and Engineering, Harbin Institute of Technology, Harbin 150001, People's Republic of China
[2] Laboratory for Space Environment and Physical Sciences, Harbin Institute of Technology, Harbin 150001, People's Republic of China

Published online: 16 April 2026

1 Introduction

The scarcity of energy resources presents a significant obstacle to achieving sustainable development in modern society [1–3]. The electrolysis of water for hydrogen production serves as a highly promising energy storage method and has been widely employed to store intermittent energy sources such as wind and solar power [4–7]. Water electrolysis involves the oxygen evolution reaction (OER) at the anode and the hydrogen evolution reaction (HER) at the cathode [8–10]. Compared to the HER, the OER exerts a more significant influence on the overall efficiency of water splitting, due to its higher energy barrier and the intrinsic complexity of the four-electron transfer process [11, 12]. During the OER, oxygen intermediates (OI) (e.g., OH*, O*, and OOH*) are formed, among which the adsorption strength of OH* is generally considered a key factor governing catalytic activity [13, 14]. A moderate adsorption strength for OI is crucial for enhancing the overall water splitting activity of a catalyst. Significant research in recent years has focused on developing electrocatalysts for water splitting, with particular emphasis on reducing the overpotential (η) [15–17], lowering costs [18–20], and enhancing stability [21, 22]. Various oxides [23–26], hydroxides [27, 28], and transition metal alloys [29–34] have demonstrated excellent performance in water splitting. In practical industrial applications, the operating performance of electrolyzers and the purity of the produced gases are strongly influenced by the quality of the feed water [35, 36]. Meanwhile, regions hosting large-scale wind and solar energy harvesting systems frequently suffer from water scarcity [37, 38]. Consequently, improving the stability of electrocatalysts under fluctuating current densities supplied by intermittent energy sources, while mitigating the adverse effects of water quality on catalytic performance, is pivotal for the practical deployment of hydrogen production via water splitting as an energy storage route.

Wastewater treatment represents an effective strategy for improving water utilization efficiency [39–41]. For instance, China's chemical oxygen demand (COD) discharge in wastewater reached 2.9544×10^7 metric tons in 2023. Wastewater treatment technologies can be broadly classified into microbial [42], physical [43], and chemical processes [44]. Notably, advanced oxidation processes (AOPs) have attracted considerable attention because of their broad industrial applicability and relatively low cost [45, 46]. The mechanism involves a catalytic chain reaction between the catalyst and oxidant. The reaction generates highly oxidative hydroxyl radicals (·OH), which enable the degradation of diverse toxic and recalcitrant organic compounds for effective wastewater treatment. Typical AOPs include electrochemical catalytic oxidation, photocatalytic oxidation, wet oxidation, and Fenton/Fenton-like processes [47, 48]. The Fenton and Fenton-like methods are particularly attractive due to their high organic degradation efficiency, absence of secondary pollution, and wide applicability [49, 50]. To reduce operational costs and extend reuse cycles, iron-based alloys have been extensively investigated as substitutes for conventional industrial iron salts [51]. However, issues such as the restriction to acidic environments, limited reusability, and relatively slow degradation kinetics remain unresolved.

If water splitting and pollutant degradation can be integrated and conducted directly in wastewater, energy storage costs can be reduced while simultaneously enabling water resource recycling. Recent studies have used of seawater [52–54] or municipal reclaimed water [55] after certain treatment to achieve water splitting. However, incomplete water degradation prevents the further recycling of water resources. In studies of OER catalysis, Liu et al. employed methanol as a probe molecule to investigate the influence of OH* adsorption strength on catalytic activity [56], explicitly defining OH* electrophilicity as being bounded by the ·OH as the upper limit and the hydroxide anion (OH^-) as the lower limit. The strong adsorption of OH* would improve the degradation efficiency of AOPs and increase the kinetic barrier of OER [57–59], suggesting that modulation of OH* adsorption strength is a feasible strategy for the development of bifunctional catalysts capable of operating in a synchronized process of AOPs

[3] Frontier Science Center for Interaction Between Space Environment and Matter, and National Key Laboratory of Space Environment and Matter Behaviors, Harbin, People's Republic of China
[4] National Key Laboratory for Precision Hot Forming, Harbin Institute of Technology, Harbin 150001, People's Republic of China
[5] School of Physics, Harbin Institute of Technology, Harbin 150001, People's Republic of China
[6] Department of Chemistry, University of South Africa, Johannesburg 1709, South Africa
[7] Department of Chemical Engineering and Biotechnology, Karshi State Technical University, 180100 Karshi, Uzbekistan
[8] School of Materials and Energy, Chongqing Key Laboratory for Advanced Materials and Technologies of Clean Energies, Southwest University, Chongqing 400715, People's Republic of China

 https://doi.org/10.1007/s40820-026-02172-1

and water splitting. A strong adsorption of OH* promotes its conversion to ·OH radicals, thereby improving the degradation rate. However, excessively strong adsorption of OH* can compromise the catalytic activity for OER. Therefore, appropriately balancing the performance of both reactions is key to developing bifunction catalysts. However, substantial challenges remain in the design of dual-function catalysts and pH regulation to enable the efficient catalysis of both reactions, thereby achieving effective conversion and recycling of energy and water resources.

Therefore, a dual-function catalyst capable of simultaneously enabling advanced oxidation and water splitting was proposed in this study. By exploiting the synergistic effects of multi-principal elements and regulating the adsorption strength for both catalytic reactions, $(FeCoNi)_{80}B_{20}$ medium-entropy amorphous alloy (MEAA) fibers were fabricated via a melt-extraction method with rapid cooling at a low material cost (~0.51 USD per gram). Owing to the crystalline–amorphous (*c*-*a*) heterostructure, the fibers exhibited exceptional degradation performance, achieving complete dye removal within 90 s and maintaining catalytic activity over more than 30 reuse cycles, while remaining effective across a broad pH range. Meanwhile, the $(FeCoNi)_{80}B_{20}$ MEAA demonstrated excellent water splitting activity, delivering η_{10} values of 275 and 220 mV for OER and HER, respectively. When employed as both anode and cathode, the electrodes maintained stable operation for 144 h under practical fluctuating current densities. In the electrolytes containing Rhodamine B (RhB), water splitting accelerated the oxidation of Fe^0 to active Fe^{3+} species and enhanced electron transport, thereby promoting faster dye degradation while preserving sufficient stability during electrolysis. Furthermore, a flow-type anion-exchange-membrane (AEM) electrolyzer assembled with $(FeCoNi)_{80}B_{20}$ MEAA as both electrodes achieved a current density of 200 mA cm^{-2} at approximately 1.96 V for over 100 h in reclaimed water, albeit with a moderate voltage increase. Structural characterization combined with density functional theory (DFT) calculations revealed that the *c*-*a* heterostructure could provide abundant active sites, whereas Fe, Co, and Ni collectively regulated OH* adsorption. Moderate OH* adsorption facilitated ·OH generation at the anode during water electrolysis, thereby enhancing degradation efficiency. The development of this bifunctional catalyst for AOPs and water splitting reduces the cost of water electrolysis for energy storage and enables resource recycling, highlighting its promising potential for industrial applications.

2 Experimental Section

2.1 Preparation of MEAA Fibers

As-cast melt-extracted was used for manufacturing a range of fibers. According to the nominal composition, a total mass of ~ 120 g of starting materials was mixed using Fe (99.99%), Co (99.99%), Ni (99.995%), and B (99.99%). These elemental powders were provided by the ZhongNuo Advanced Material Technology Co. Ltd., China. Analytical-grade chemical reagents were all utilized immediately, without any additional purification. The beginning materials were smelted 4–5 times using vacuum arc smelting to guarantee that the components are evenly combined while being shielded by high-purity argon (99.999%). Then, the metal rod (about 2–3 cm) was melted in a high-purity BN crucible, and the resulting solution was dipped in oxygen and discarded as soon as the copper wheel began to rotate and met the molten surface. The alloy rod was melted by applying a current of approximately 22.5 A and then fed toward the copper wheel at a constant speed of 30 μm s^{-1}. The copper wheel rotated at a surface velocity of 1700 r min^{-1}. Upon contact with the wheel, the molten alloy underwent rapid solidification due to the large temperature gradient and was subsequently spun off to form continuous fibers. Ultimately, HEA fibers measuring around 3–4 cm in length, 30–35 μm in diameter, and ~ 115 g in total mass were produced. Among all the elements, aluminum corrodes the easiest. To increase the specific surface area, porous morphological characteristics were realized via a typical dealloying corrosion strategy in 1.0 M HCl. After dealloying, the as-obtained fibers were successively cleaned by absolute ethyl alcohol (99.5%) and distilled water (18.2 MΩ cm) for 30 min. The mixing entropy of the alloys was calculated by using:

$$\Delta S_{mix} = -R \sum x_i \ln x_i \quad (1)$$

where R is the gas constant and x_i is the atomic (or mole) fraction of component.

The mixing entropy of $(FeCoNi)_{80}B_{20}$ is approximately 1.38R that meet the definition of medium-entropy alloys [60, 61].

2.2 Physical Characterization

The morphology of fibers was characterized by field-emission scanning electron microscopy (FE-SEM) and transmission electron microscopy (TEM). Scanning electron microscopy (SEM) observations were made using the Carl Zeiss Merlin Compact and TEM analysis was conducted using an FEI Talos F200s, operating at 200 kV. The electron back scatter Raman spectra were collected using a LabRAM HR Evolution. X-ray photoelectron spectroscopy (XPS) was carried out using a ThermoFisher Scientific Esca Xi+, equipped with Al Kα radiations (1486.6 eV). The inductively coupled plasma-optical emission spectrometry (ICP-OES) was measured using Thermo iCAP 740.

2.3 Catalytic Experiments of Degradation

Both as-prepared fibers were employed as catalysts for PS activation. RhB, SM2, and benzothiazole were used as target pollutants, and residual concentrations were measured via high-performance liquid chromatography (HPLC Scion LC6000). The detection wavelengths were 550 nm for RhB, 270 nm for SM2, 270 nm for phenol, and 245 nm for benzothiazole, respectively, with mobile phase as follows: methanol and 0.1% formic acid solution (70: 30, V: V), acetonitrile and 0.1% formic acid solution (30: 70, V: V), and methanol and 0.1% formic acid solution (45: 55, V: V), respectively. Unless stated otherwise, the catalyst amount was 0.5 g L^{-1}, pollutant and PS concentration were 25 mg L^{-1} and 10 mm, respectively. Moreover, experiments were conducted at ambient temperature with a pH of 5.0. For each test, 100 mL of aqueous pollutant solution was prepared, and catalysts were dispersed within it. Upon the addition of PS, the reaction start time was recorded. Samples of 4 mL were collected at predetermined intervals, passed through a 0.22 μm pore-sized filter membrane, and analyzed using HPLC and TOC measurements. The kinetic rate constant (k_{obs}) was calculated by using:

$$\ln(C_0/C_t) = k_{obs} \quad (2)$$

where C_0 is the original concentration of the pollutant and C_t is the concentration of the pollutant at time t.

To evaluate catalyst stability, samples underwent ultrasonic cleaning in ultrapure water and ethanol between cycles and reused. Radical types were confirmed using an ESR/EPR (Brook EMX Plus).

2.4 Electrochemical Measurements

Electrochemical measurements were conducted using an electrochemical working station (CHI 760E) in a three-electrode setup, where 1 M KOH solution was used as an electrolyte, an Hg/HgO electrode (in 1 M KOH) was used as a reference electrode and the graphite rod (99.9%, with a diameter of 8 mm) was used as a counter electrode. Oxygen evolution reaction (OER) overpotential (η) was calculated using the following relationship:

$$E(RHE) = E(Hg/HgO) + 0.059pH + 0.098 \quad (3)$$

LSV and Tafel curves were corrected by 95% iR compensation for the ohmic loss except for AEM test. Electrochemical impedance spectroscopy (EIS) was carried out at 1.58 V in the frequency range of 1000 kHz to 10 mHz with an amplitude of 5 mV. EIS analysis was carried out by fitting the Nyquist plot using an equivalent circuit, which was realized by the Z-view software. Chronopotentiometry measurements were performed to evaluate the long-term stability. The electrochemical surface area (ECSA) was determined by measuring the capacitive current associated with double-layer charging from five different scan-rates (10, 30, 50, 70, 90, and 110 mV s^{-1}). In these regions, the integrated charge should be due to the charging of the electrode–electrolyte double layer. The double-layer charging current (i), normalized on the geometric area of the electrode, is directly proportional to the scan rate (υ), i.e., $i = \upsilon C_{dl}$. By drawing the curves of anodic and cathodic currents with respect to the scan rate, the average C_{dl} of linear fitting slope is derived. The measured capacitance currents are plotted as a function of the scan rate, as shown in Fig. S15. According to the reported typical value, the specific capacitance (C_s) of electrocatalyst in 1 M KOH is selected as $C_s = 0.040$ mF cm^2. Therefore, the ECSA of the catalyst layer can be calculated using Eq. (4):

$$ECSA = C_{dl}/C_s \quad (4)$$

About 10 fibers were arranged in parallel function and employed as catalyst materials for the anode and cathode in AEM. The active area corresponds to the collective geometric surface area of the fibers (assumed as cylinder). The electric conduction and electrolyte transport are performed by S-type Ti current collectors with a serpentine flow field. The AEM electrolyzer was put together with the cathode or anode compartment first, followed by the end plate, sealing gasket, Ti current collector, fibers, and sealing gasket. An anion-exchange

https://doi.org/10.1007/s40820-026-02172-1

membrane (Fumasep FAA-3-PK-130) was employed to divide the electrolyzer's cathode and anode compartments. A peristaltic pump was used to regulate the flow of the simulated wastewater (1.0 M KOH with 25 mg L^{-1} RhB) electrolyte to both sides of the electrolyzer at a rate of 2.5 mL min^{-1} throughout the testing.

2.5 Theoretical Calculations

All the calculations are performed in the framework of the density functional theory with the projector augmented plane wave method, as implemented in the Vienna ab initio simulation package (VASP). The generalized gradient approximation (GGA) proposed by Perdew, Burke, and Ernzerhof (PBE) is selected for the exchange–correlation potential. The long-range van der Waals interaction is described by the DFT-D3 approach. The cutoff energy for plane wave is set to 480 eV. The energy criterion is set to 10−4 eV in iterative solution of the Kohn–Sham equation. All the structures are relaxed until the residual forces on the atoms have declined to less than 0.05 eV $Å^{-1}$. Data analysis and visualization are carried out with the help of VASPKIT6 code and VESTA7. A 2×2×1 k-point mash in Brillouin zone was applied in this case. The system was equilibrated and analyzed in the NVT ensemble (constant particle number, volume, and temperature) at a temperature of 1000 K. A time step of 3 fs was employed to ensure accurate integration of the equations of motion. To avoid interlaminar interactions, a vacuum spacing of 20 Å is applied perpendicular to the slab.

Here, differences in Gibbs free energy (ΔG) for intermediates defined as:

$$\Delta G = \Delta E + \Delta EZPE - T\Delta S \quad (5)$$

where ΔG is the total energy difference between the slab and respective terminations computed by DFT-PBE. ΔEZPE and TΔS denote differences in zero-point energy and entropy between adsorbed states of reaction intermediates and gap phase, respectively. T is the room temperature (298.15 K).

3 Results and Discussion

3.1 Exploration of Combination of AOPs and Water Splitting

In industrial applications, water electrolysis for hydrogen production represents an essential route for energy storage. However, water splitting is constrained by high energy consumption and stringent water quality requirements, while regions characterized by large-scale deployment of wind and solar energy harvesting systems often experience persistent water scarcity, thereby increasing costs and hindering practical implementation (Fig. 1). Hence, we proposed a "water-energy nexus" strategy. Performing overall water splitting directly in wastewater or reclaimed water while simultaneously achieving pollutant degradation can markedly enhance energy utilization efficiency and promote resource recycling. Accordingly, the combination of AOPs with water splitting is considered promising for several reasons (inset in Fig. 1). (1) Water relevance: The treated water can be directly reused for electrolytic hydrogen production. (2) Power consumption: The electrical energy applied during electrolysis can accelerate degradation kinetics. (3) Active elements: The active sites for both catalytic reactions can be primarily associated with transition metals. (4) Intermediates: Similar reaction intermediates can be involved and mutually transformed by regulating OH* adsorption. Although the optimal pH ranges for the two reactions are slightly different and require further optimization, this integrated route offers a practical strategy for stable storage of intermittent renewable energy in the form of hydrogen while enabling the direct utilization of reclaimed water. Consequently, the central challenge lies in the design of a bifunctional catalyst for AOPs and water splitting that delivers high catalytic performance under suitable pH conditions and a balance of activity for AOPs and water splitting. In this context, $(FeCoNi)_{80}B_{20}$ MEAA are regarded as promising bifunctional catalysts [62–64], as they contain Fe and Co active sites favorable for AOPs, along with Fe, Co, and Ni sites that are active for water splitting. The OH* binding strength follows the order Ni > Co > Fe [56]. The simultaneous incorporation of Fe, Co, and Ni enables the modulation toward a moderate OH* adsorption strength, thereby imparting bifunctional catalytic capability of AOPs and water splitting to $(FeCoNi)_{80}B_{20}$ in a synchronized process. In addition, the introduction of small-radius B enhances the glass-forming ability of MEAA, contributing to broadening the applicable pH window for catalytic operation.

3.2 Electrocatalyst Synthesis and Characterization

$(FeCoNi)_{80}B_{20}$ fibers along with a series of control samples were prepared via a melt-extraction method with a high cooling rate to construct a *c*-*a* heterostructure [65–68]. A substantial quantity of fibers (~ 100 g) was produced in a

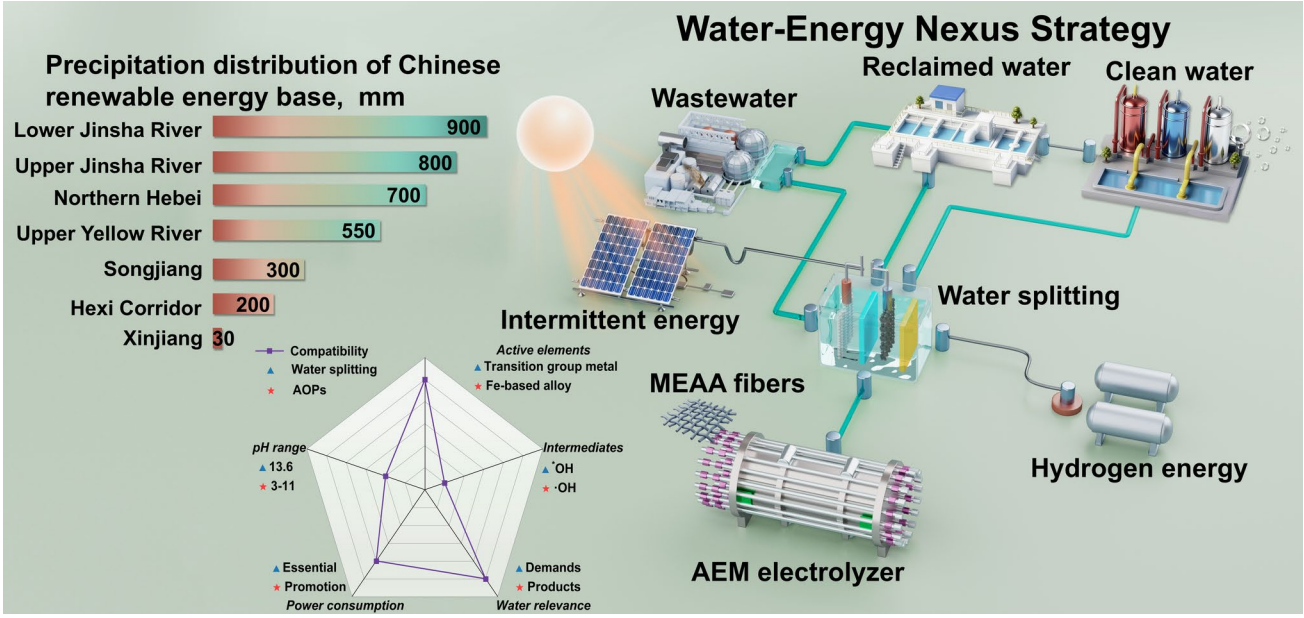

Fig. 1 Conceptual illustration of the water–energy nexus strategy. Regions with large-scale solar and wind energy harvesting systems often experience severe water scarcity. The proposed system integrates energy storage and water purification through water splitting, coupled with advanced oxidation processes (AOPs). When using water electrolysis for hydrogen production to store intermittent energy sources, wastewater and reclaimed water can be directly introduced into the electrolyzer after simple physical filtration and adsorption. This integrated process enables stable oxygen evolution while simultaneously achieving effective water purification, thereby enhancing energy utilization efficiency and resource recycling. Inset: Radar chart illustrating the compatibility between water splitting and AOPs. Water splitting and AOPs exhibit compatibility in aspects active elements, intermediates, water relevance, power consumption, and pH range. This compatibility enables the integration of both reactions and suggests a design strategy for dual-function catalysts

single batch (Fig. S1), resulting in a competitive cost of approximately 0.51 USD per gram with accurate composition and high quality [69–73], and indicating considerable potential for industrial application. Scanning electron microscopy (SEM) images revealed that the $(FeCoNi)_{80}B_{20}$ MEAA fibers possessed diameters of approximately 30 μm with smooth surfaces, while energy-dispersive X-ray spectrometry (EDS) mapping confirmed a uniform elemental distribution on the surface (Figs. 2f and S2). The X-ray diffraction (XRD) patterns (Fig. 2a) exhibited evident structural differences among the samples. $Fe_{80}B_{20}$ displayed a single broad diffraction peak characteristic of an amorphous structure. In contrast, the XRD pattern of $(FeCoNi)_{80}B_{20}$ demonstrated sharp nanocrystalline peaks corresponding to Fe_3B (ICDD-PDF-2, PDF card no. 39–1315) and an amorphous feature still exists on the XRD patterns, indicating the construction of a partially crystallized state (or amorphous/crystalline structure) [74]. The $Fe_{25}Ni_{75}$ and $Fe_{33}Co_{33}Ni_{34}$ exhibited crystalline structures with a characteristic Ni_3Fe phase (ICDD-PDF-2, card no. 88–1715). The surface chemical states of the as-prepared $(FeCoNi)_{80}B_{20}$ were examined using X-ray photoelectron spectroscopy (XPS). The Fe 2*p* spectrum was deconvoluted into Fe^0, Fe^{2+}, and Fe^{3+} components, with Fe $2p_{3/2}$ binding energies of 707.2, 709.7, and 711.9 eV, respectively (Fig. 2b). Compared with Fe^{2+} and Fe^{3+}, the relatively higher proportion of Fe^0 could facilitate electron transfer and enhance the catalytic performance during degradation. The Co 2*p* spectrum was resolved into Co^0, Co^{2+}, and Co^{3+} species, with corresponding $2p_{3/2}$ binding energies of 780.1, 781.4, and 785.7 eV (Fig. 2c). For the active Ni sites associated with water splitting, Ni^0 was predominant (Fig. 2d), suggesting the transformation to catalytically active Ni^{3+} during operation. The O 1*s* spectrum indicated the presence of M–O and M-OH bonds (Fig. 2e), while the B 1*s* spectrum confirmed the existence of B-B and B-O bonds (Fig. S3).

Cross-sectional transmission electron microscopy (TEM) analysis sample was prepared using an ion-milling technique (Fig. S4) and the TEM images revealed a distinct *c-a* heterostructure. High-resolution TEM (HRTEM, Fig. 2g) combined with the selected area electron diffraction (SAED) pattern (inset in Fig. 2g) demonstrated that the amorphous

 https://doi.org/10.1007/s40820-026-02172-1

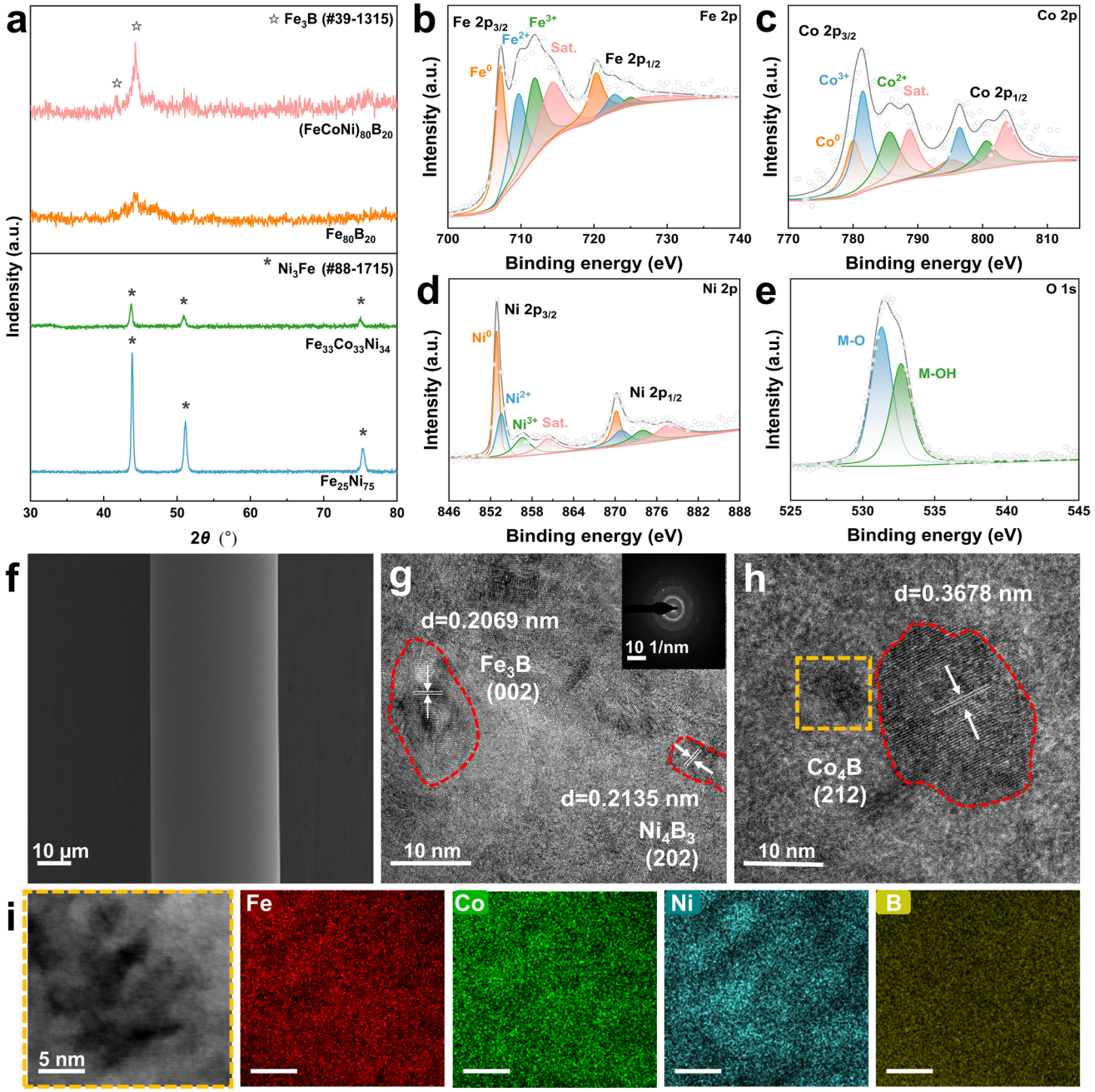

Fig. 2 Structural characterization of $(FeCoNi)_{80}B_{20}$ ME-MGs. **a** X-ray diffraction patterns of $Fe_{80}B_{20}$, $Fe_{75}Ni_{25}$, $Fe_{33}Co_{33}Ni_{34}$, and $(FeCoNi)_{80}B_{20}$. XPS spectra of **b** Fe 2*p*, **c** Co 2*p*, **d** Ni 2*p*, and **e** O 1*s*. **f** SEM image of the as-prepared fibers. **g** HRTEM image (inset: corresponding SAED pattern with polycrystalline rings), where a red dashed circle is used to highlight the nanocrystallites of Fe and Ni borides that are approximately 10–15 nm in size. **h** HRTEM image of Co boride nanocrystallites with a size of approximately 20 nm. **i** EDS analysis of the yellow square frame region in **h**

matrix contained nanocrystalline Fe_3B, Ni_4B_3, and Co_4B phases with interplanar spacings of 0.2069, 0.2135, and 0.3678 nm, corresponding to the (002), (202), and (212) facets, respectively. Nanocrystalline domains with sizes of approximately 10–20 nm are generally regarded as the active species for both AOPs and water splitting and presents in large quantities (Fig. S5), corresponding well to the crystalline peaks observed in the XRD pattern. Furthermore, EDS elemental mapping (Fig. 2i) of the yellow square frame

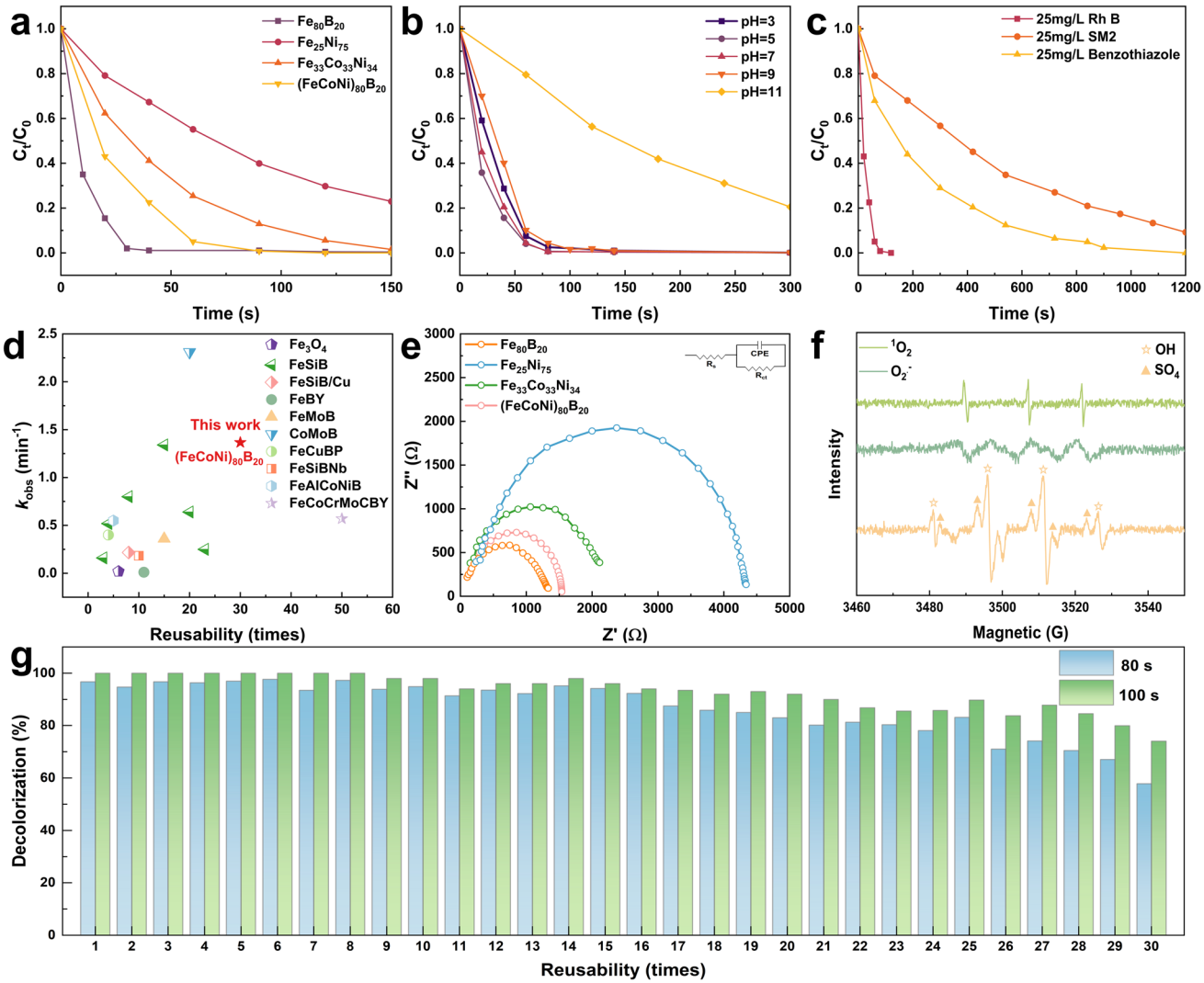

Fig. 3 AOP catalytic activity and stability. **a** Degradation efficiency of samples in the presence of 10 mM PS. Degradation efficiency of $(FeCoNi)_{80}B_{20}$ fibers **b** under different pH conditions and **c** for various organic pollutants. **d** Comparison of the degradation capacity of $(FeCoNi)_{80}B_{20}$ with other reported catalysts, as summarized in Table S1. **e** Nyquist plots of the catalysts measured in 25 mg L^{-1} RhB solution. **f** ESR experiments on $(FeCoNi)_{80}B_{20}$. **g** Reusability of $(FeCoNi)_{80}B_{20}$ fibers

region in Fig. 2h confirmed a homogeneous elemental distribution throughout the *c*-*a* heterostructure and the amorphous base exhibited a uniform elemental distribution (Fig. S6). These observations verified the successful construction of the *c*-*a* heterostructure, which improved the erosion resistance and increased the density of active sites.

3.3 AOPs Catalytic Performance

The catalytic performance of the samples was tested using a 25 mg L^{-1} RhB solution. As shown in Fig. 3a, $Fe_{80}B_{20}$ and $(FeCoNi)_{80}B_{20}$ achieved nearly complete decolorization within 30 and 90 s, respectively. Because stability is a critical parameter for AOPs, the reusability of $Fe_{80}B_{20}$ and $(FeCoNi)_{80}B_{20}$ was further examined. The $(FeCoNi)_{80}B_{20}$ fibers remained effective for up to 30 reuse cycles, with only a slight decrease in efficiency thereafter (Fig. 3g), whereas $Fe_{80}B_{20}$ maintained its activity for 25 cycles (Fig. S7). These results indicated that $(FeCoNi)_{80}B_{20}$ exhibited superior AOPs performance by combining high degradation efficiency with enhanced reuse stability (Fig. 3d). To assess the influence of solution pH on degradation behavior, $(FeCoNi)_{80}B_{20}$ fibers were tested over a pH range of 3–11

 https://doi.org/10.1007/s40820-026-02172-1

(Fig. 3b). The fastest decolorization was observed at pH 5, exceeding that of conventional Fe-based catalysts. Notably, even at pH 11, more than 80% decolorization was achieved within 300 s, demonstrating pronounced pH adaptability. In addition, $(FeCoNi)_{80}B_{20}$ enabled the effective degradation of sulfadimethylpyrimidine (SM2) and benzothiazole, achieving removal efficiencies of 100% and 92% within 1200 s, respectively (Fig. 3c). The effects of environmental parameters, including temperature, catalyst dosage, and RhB concentration, were also investigated (Fig. S8a–c), and the optimal operating conditions were identified as a catalyst loading of 0.5 g L^{-1}, an RhB concentration of 25 mg L^{-1}, and ambient temperature.

To assess the extent of metal leaching into the contaminant solution, the inductively coupled plasma–optical emission spectroscopy (ICP–OES) was employed after reaction (Fig. S9). During degradation, the leaching of Fe, Co, and Ni was detected, with Fe exhibiting the most pronounced release, indicating that a greater number of Fe sites participated in the catalytic process. This result corresponded the recent researches that Fe played the dominant role as the primary active site in AOPs [75–77]. Electron spin resonance (ESR) spectroscopy confirmed the generation of ·OH, $SO4^{-}$, O_2^{-}, and $^1O_2$ species during the degradation process (Fig. 3f). The ESR signals revealed abundant ·OH and $SO_4{\cdot}^{-}$ radicals, whereas only minor amounts of O_2^{-} and $^1O_2$ were detected, highlighting the dominant contribution of radical pathways to pollutant degradation [78, 79]. Furthermore, quenching experiments results of $(FeCoNi)_{80}B_{20}$ fibers using furfuryl alcohol (FFA), p-Benzoquinone, methyl alcohol (MeOH), and tertiary butanol (TBA) as quenching agents (Fig. S10). The efficiency exhibited obviously decreased with the addition of the TBA and MeOH that demonstrated that the pivotal role of ·OH and $SO4^{-}$generated radicals in organic molecule degradation. FFA and p-Benzoquinone were used to detect the production of O_2^{-} and $^1O_2$ radicals. The results indicated the small amounts of O_2^{-} and $^1O_2$ species were produced during the water treatment processes. The results of the quenching experiments were corresponded to the ESR results. Electron transfer characteristics were further examined by electrochemical impedance spectroscopy (EIS) in 25 mg L^{-1} RhB solution (Fig. 3e). The Nyquist plots and fitted equivalent circuits of $(FeCoNi)_{80}B_{20}$ exhibited a relatively a lower charge-transfer resistance (R_{ct} = 1443 Ω) than those of $Fe_{80}B_{20}$ (R_{ct} = 1259 Ω), $Fe_{33}Co_{33}Ni_{34}$ (R_{ct} = 2048 Ω), and $Fe_{75}Ni_{25}$ (R_{ct} = 4191 Ω), which was consistent with the observed degradation performance. Electrochemical polarization analysis using the Tafel extrapolation method (Fig. S11) revealed that $(FeCoNi)_{80}B_{20}$ possessed the lowest self-corrosion current density (I_{corr} = 0.0046 mA cm^{-2}), indicating superior corrosion resistance. This enhanced corrosion resistance accounted for the improved reusability and collectively highlights the advantages of the *c-a* heterostructure. To elucidate the origin of the gradual decline efficiency after prolonged cycling, the SEM images of $(FeCoNi)_{80}B_{20}$ fibers after 30 degradation cycles were analyzed. The fiber surface exhibited extensive spalling accompanied by precipitate formation (Fig. S12). The corresponding EDS mapping revealed that these precipitates were primarily composed of Fe, C, and O (Fig. S13), which was identified as the main cause of catalyst deactivation.

3.4 Water Splitting Catalytic Performance

The electrochemical activities of different samples were tested in 1.0 M KOH. For OER, linear sweep voltammetry (LSV) curves illustrate that $Fe_{33}Co_{33}Ni_{34}$ and $(FeCoNi)_{80}B_{20}$ delivered superior catalytic performance, with η_{10} values of 288 and 275 mV, respectively (Fig. 4a). In contrast, $Fe_{80}B_{20}$ exhibited negligible OER activity and was therefore not considered for further analysis. The $(FeCoNi)_{80}B_{20}$ catalyst displayed a Tafel slope of 53.45 mV dec^{-1}, comparable to that of $Fe_{75}Ni_{25}$ (53.50 mV dec^{-1}) and $Fe_{33}Co_{33}Ni_{34}$ (45.26 mV dec^{-1}) (Fig. 4b). As summarized in Fig. 4c, $(FeCoNi)_{80}B_{20}$ exhibited competitive OER activity compared with representative catalysts based on transition and noble metals. The EIS measurements yielded Nyquist plots that were fitted using a Randles equivalent circuit (Fig. S14). Among the tested samples, $(FeCoNi)_{80}B_{20}$ demonstrated the lowest charge-transfer resistance (R_{ct} ≈ 76.2 Ω), which was markedly lower than those of $Fe_{80}B_{20}$ (≈79.4 Ω), $Fe_{75}Ni_{25}$ (≈335.0 Ω), and $Fe_{33}Co_{33}Ni_{34}$ (≈376.4 Ω), indicating the accelerated Faradaic processes [80]. The electrochemical surface area (ECSA) estimated from the double-layer capacitance (C_{dl}) obtained by cyclic voltammetry (CV) (Fig. S15) revealed that $(FeCoNi)_{80}B_{20}$ possessed the highest C_{dl} value (0.209 mF cm^{-2}), significantly exceeding those of $Fe_{75}Ni_{25}$ (0.022 mF cm^{-2}) and $Fe_{33}Co_{33}Ni_{34}$ (0.098 mF cm^{-2}), suggesting a higher density of exposed active sites.

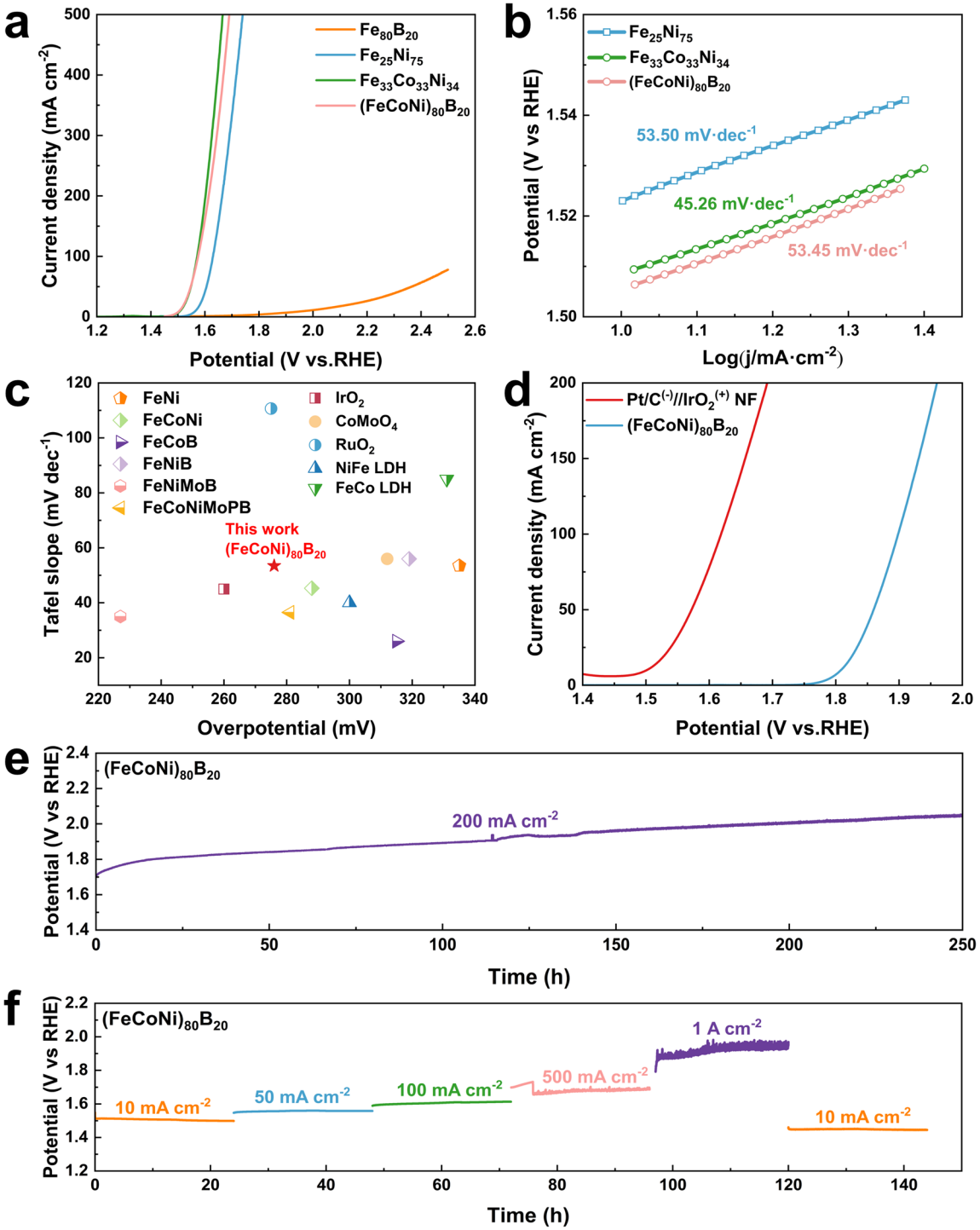

Fig. 4 Water splitting catalytic activity and stability. **a** LSV curves for four samples evaluated in 1.0 M KOH (iR corrected, scan rate: 5 mV s^{-1}). **b** Corresponding Tafel slopes. **c** Comparison of the overpotential and Tafel slope of $(FeCoNi)_{80}B_{20}$ with other reported catalysts, as summarized in Table S2. **d** Comparison of overall water splitting activity of $(FeCoNi)_{80}B_{20}$ with Pt/C//IrO_2 Ni foam electrolyzer. **e** Chronopotentiometry curves of $(FeCoNi)_{80}B_{20}$ recorded at a current density of 200 mA cm^{-2}. **f** Chronopotentiometry curves of $(FeCoNi)_{80}B_{20}$ under practical fluctuating current densities (10, 50, 100, 500, 1000, and 10 mA cm^{-2})

https://doi.org/10.1007/s40820-026-02172-1

The electrochemical stability was assessed by chronopotentiometry at a current density of 1 A cm^{-2} (Fig. S16), and $(FeCoNi)_{80}B_{20}$ maintained stable operation for 120 h with only a modest increase in potential. For HER, the η_{10} for $Fe_{80}B_{20}$, $Fe_{75}Ni_{25}$, $Fe_{33}Co_{33}Ni_{34}$, and $(FeCoNi)_{80}B_{20}$ were 433, 406, 399, and 222 mV, respectively (Fig. S17a). In addition, $(FeCoNi)_{80}B_{20}$ exhibited the lowest Tafel slope and R_{ct} among the samples (Fig. S17b, c), demonstrating favorable HER kinetics and enhanced electron transfer capability [81]. The $(FeCoNi)_{80}B_{20}$ used as both cathode and anode was further evaluated the overall water splitting performance. As shown in Fig. 4d, the cell voltage of was 1.96 V to reach a current density of 200 mA cm^{-2}, which was higher than that of noble-metal-based catalysts but remained competitive with non-precious systems. Notably, the $(FeCoNi)_{80}B_{20}$-based electrolyzer operated stably for 250 h at 200 mA cm^{-2} (Fig. 4e) with increased voltage and maintained its durability for 144 h under simulated industrially relevant fluctuating current densities (Fig. 4f). The overall water splitting reaction was conducted in a membrane-free cell, which led to local pH shifts that would increase the kinetic overpotential of the electrode reactions [82]. Thus, the cell voltage increased before reaching stability. The ICP-OES results (Table S3) exhibited significant leaching of the active elements element after 250 h stability test at 200 mA cm^{-2} that may contribute to the observed activity degradation. At the same time, the fiber surface remained smooth and self-supporting (Fig. S18), with uniformly distributed surface elements (Fig. S19). The TEM characterization was preformed to furtherly explore the reasons for the sharp decline in stability. The HRTEM image revealed a substantial reduction in nanocrystal size after prolonged stability testing (Fig. S20). This is another reason for the limited stability because the nanocrystalline exhibited better activity for water splitting [65, 83].

3.5 Water Splitting Catalytic Performance in Reclaimed Water

Based on the AOPs and water splitting catalytic properties of $(FeCoNi)_{80}B_{20}$, these two processes can be conducted simultaneously. Overall water splitting was performed at a current density of 200 mA cm^{-2} in simulated reclaimed water (1.0 M KOH with 25 mg L^{-1} RhB). Complete decolorization of the solution was achieved within 60 min, whereas the water splitting process maintained stable operation for approximately 115 h (Figs. 5a and S21a). The total organic carbon (TOC) removal rate reached 63.24% (Fig. 5b). Compared with conventional decolorization, the synchronized process exhibited higher degradation efficiency. The presence of RhB and $Na_2S_2O_8$ exerted only a negligible influence on OER performance (Fig. S22a, b), whereas the decolorization efficiency was significantly accelerated under an applied current owing to enhanced electron transfer (Fig. S22c) [84]. The ICP–OES analysis revealed the leaching behavior of Fe, Co, and Ni after the two processes (Table S4). The higher Fe leaching rate observed in the synchronized process was attributed to the more rapid oxidation of Fe^0 during water splitting, which promoted the degradation reaction. The XPS spectra collected after AOPs, water splitting, and synchronized process exhibited no substantial changes in peak features, indicating the structural stability of $(FeCoNi)_{80}B_{20}$ under different operating conditions (Fig. S23a–c). Notably, the Fe 2*p* (Fig. S24a) and Ni 2*p* (Fig. S24b) spectra displayed the evident negative shifts after the synchronized process, suggesting an increased electron density around Fe and Ni atoms, which is beneficial for catalytic activity [85]. Furthermore, the synchronized process resulted in the highest proportions of M–OH and M–OOH species (Fig. S23c), implying the generation of a greater number of active sites. Raman spectroscopy was employed to probe the variations of active species in the surface during different catalytic processes (Fig. S25). Compared with the other samples, the fiber after the synchronized process exhibited enhanced Raman bands at 281, 472, 554, and 715 cm^{-1}, which were characteristic of FeOOH [86] and NiOOH [15], indicating the formation of the active M-OOH species during operation. These results were consistent with the XPS results.

To assess practical applicability, an AEM electrolyzer was assembled using $(FeCoNi)_{80}B_{20}$ as both anode and cathode in simulated reclaimed water (Fig. S26). The AEM electrolyzer sustained a current density of 200 mA cm^{-2} for approximately 100 h (Fig. 5c). Compared with recent amorphous alloy researches, the $(FeCoNi)_{80}B_{20}$ maintained electrocatalytic activity for water splitting in reclaimed water while simultaneously achieving efficient reclaimed water purification (Table S5). The XRD patterns were tested to further demonstrate the stability (Fig. S27). The crystalline peaks became less sharp after the synchronized process, suggesting the occurrence of structural reconstruction during the process. The LSV curves before and after the 100 h stability

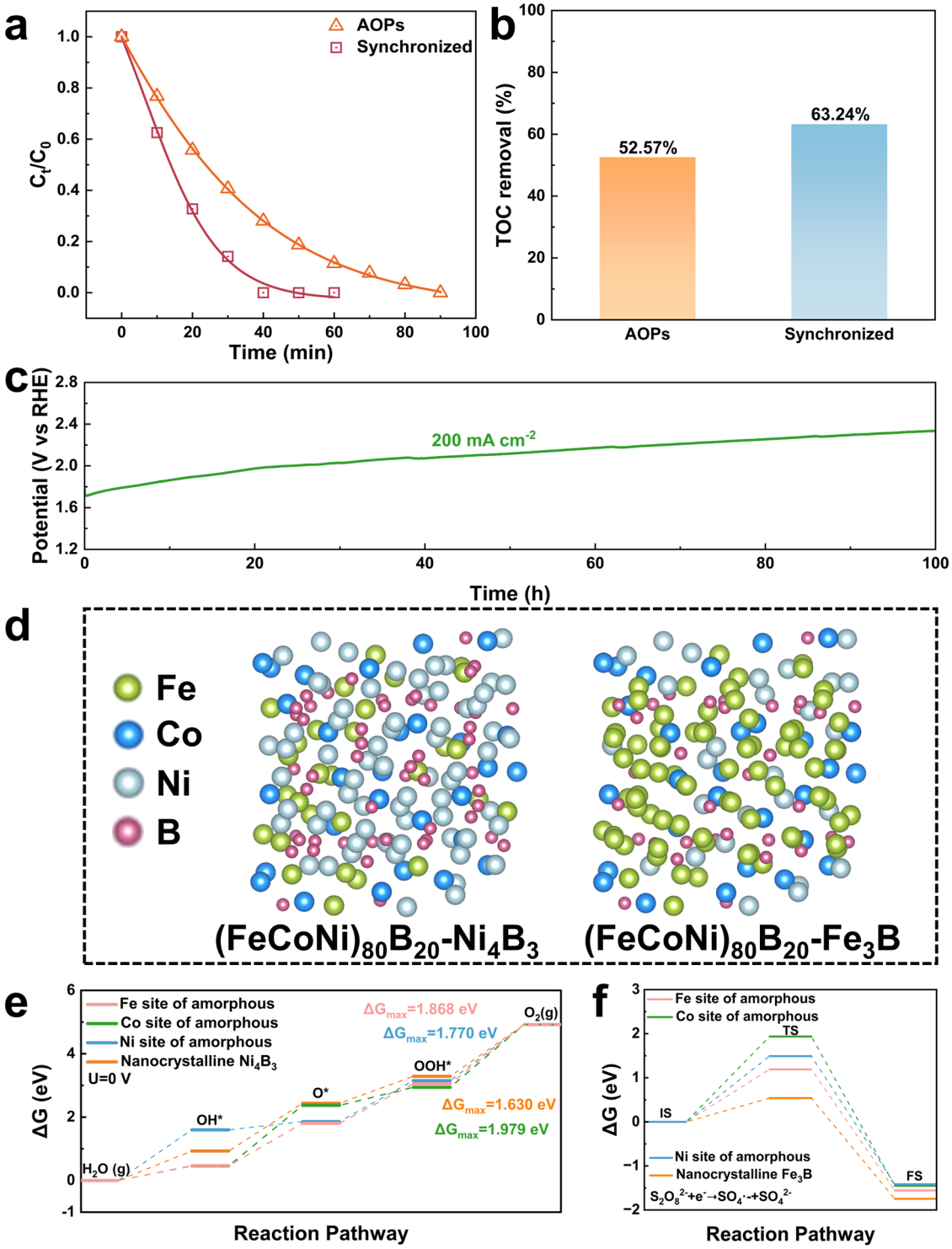

Fig. 5 Synchronized catalytic activity and stability of the integrated AOPs–water splitting process. **a** Degradation efficiency of $(FeCoNi)_{80}B_{20}$ in simulated reclaimed water (1.0 M KOH + 25 mg L^{-1} RhB) under simultaneous overall water splitting at a current density of 200 mA cm^{-2}. **b** Comparison of TOC removal rates between AOP-only process and annealed synchronized process. **c** Chronopotentiometry curve of the AEM electrolyzer operated at a current density of 200 mA cm^{-2} in simulated reclaimed water (without iR correction). **d** Calculation models of *c-a* for $(FeCoNi)_{80}B_{20}$-Ni_4B_3 and $(FeCoNi)_{80}B_{20}$-Fe_3B. **e** Gibbs free energy changes for the four steps in the OER process at Fe, Co, and Ni site of the amorphous $(FeCoNi)_{80}B_{20}$ and nanocrystalline Ni_4B_3. **f** Calculated energy profile for $S_2O_8^{2-}$

https://doi.org/10.1007/s40820-026-02172-1

tests were implied to confirm the stability (Fig. S28). The overpotential increased 17 mV at 10 mA cm^{-2} that demonstrated the great stability in the synchronized process. In contrast, when operated after decolorization alone, $(FeCoNi)_{80}B_{20}$ remained stable for only approximately 75 h at 200 mA cm^{-2}, which was significantly shorter than that observed in the synchronized process (Fig. S21b). The SEM images obtained after 115 h of synchronized operation demonstrated that the fibers retained their self-supporting structure, while abundant surface precipitates were observed (Fig. S29a). EDS mapping confirmed that these precipitates were primarily composed of Fe, C, and O (Fig. S29b). Compared with fibers after decolorization, no pronounced surface flaking was detected, which may contribute to the improved stability during subsequent water splitting operations. The combined catalytic activity and durability demonstrated in the synchronized process highlights the feasibility of this strategy for industrial applications.

3.6 Mechanism Investigation for Bifunctional Catalyst

The adsorption behavior of OH* was examined by leading methanol into the electrolyte (Fig. S30a–c). The difference in current density induced by the methanol oxidation reaction (MOR) can be used as an indicator of the extent of surface OH* accumulation [87]. Stronger OH* binding favors a higher decolorization rate, whereas moderate binding strength is more conducive to efficient water splitting. Owing to its moderate OH* adsorption energy, $(FeCoNi)_{80}B_{20}$ facilitated the generation of ·OH at the anode during the synchronized process, thereby enhancing the degradation efficiency. The process in which applied voltage drives the single-electron oxidation of water to generate highly oxidative •OH is referred to as EOPs. Meanwhile, because an oxidant was added to the simulated wastewater, AOPs can also occur in the absence of applied voltage. This behavior indicated a coupled reaction pathway in which AOPs and EOPs proceeded simultaneously, resulting in accelerated degradation kinetics [57].

Because Fe and Ni sites serve as the primary active centers for AOPs and overall water splitting, respectively, the structural models of *c-a* $(FeCoNi)_{80}B_{20}$-Ni_4B_3 and $(FeCoNi)_{80}B_{20}$-Fe_3B were constructed based on TEM observations (Fig. 5d). According to the Gibbs free energy changes (ΔG) calculated for the OER four-electron pathway on amorphous $(FeCoNi)_{80}B_{20}$ and nanocrystalline Ni_4B_3 for OER 4e^- pathway (Fig. S31), the rate-determining step on the Fe, Co, and Ni site at 0 V corresponded to the oxidation of *OOH to O_2, with ΔG_{max} values of 1.868, 1.979, 1.770, and 1.630 eV, respectively (Fig. 5e). Compared with the amorphous substrate, nanocrystalline Ni_4B_3 exhibited a markedly lower ΔG_{max} with an increased OH desorption energy, which accounted for its superior catalytic activity toward both OER and AOPs. To elucidate the activation pathway of $S_2O_8^{2-}$, transition-state simulations were performed for amorphous $(FeCoNi)_{80}B_{20}$ and nanocrystalline Fe_3B (Fig. S32). The nanocrystalline Fe_3B displayed a substantially lowest energy barrier (0.539 eV) (Fig. 5f) and the Fe site exhibited the lower barrier (1.191 eV) at the amorphous phase that is consistent with the results of degradation experiments. In addition, the final state of the interfacial activation process exhibited relative energies of − 2.749 and − 2.285 eV for amorphous $(FeCoNi)_{80}B_{20}$ and nanocrystalline Fe_3B, respectively, indicating that the heterolytic cleavage of $S_2O_8^{2-}$ occurred more readily on nanocrystalline Fe_3B. Compared with the amorphous matrix, the nanocrystalline domains exhibited enhanced activity for both processes, highlighting the advantage of the crystalline–amorphous heterostructure. The total density of states (TDOS) analysis of amorphous $(FeCoNi)_{80}B_{20}$, $(FeCoNi)_{80}B_{20}$-Ni_4B_3, and $(FeCoNi)_{80}B_{20}$-Fe_3B revealed that the Ni sites increased the density of empty states near the Fermi level, indicating the presence of abundant unpaired electrons associated with Ni (Fig. S33a–c) [88]. Partial density of states (pDOS) analysis further indicated that Fe, Co, and Ni sites collectively regulated the adsorption characteristics of $(FeCoNi)_{80}B_{20}$, thereby facilitating intermediate desorption in both catalytic reactions. The partial radial distribution functions (PRDFs) of Fe, Co, and Ni in $(FeCoNi)_{80}B_{20}$ are shown in Fig. S34. The lower PRDF peak intensities corresponded to lower coordination numbers, which favored the generation of additional active sites [89]. The analysis of the first PRDF peak reveals the specific coordination number for each sample [90]. Notably, the Fe–Ni pair exhibited the lowest peak intensity, suggesting that the interaction between Fe and Ni sites plays an important role in improving the activity of both AOPs and water splitting. Overall, the DFT results demonstrated that Fe and Ni sites were intrinsically beneficial for the two catalytic processes, while the *c-a* heterostructure increased the number of active

sites, and the nanocrystalline domains further enhanced the catalytic activity.

4 Conclusion

In this study, a bifunctional catalyst integrating AOPs and water splitting was developed and demonstrated to operate effectively in reclaimed water. The synergistic interaction among multiple elements and the stable amorphous structure of MEAA enabled the integration of both reaction pathways, while the modulation of oxygen intermediate binding strength achieved a balance between the two functionalities. As a result, the $(FeCoNi)_{80}B_{20}$ catalyst exhibited outstanding catalytic activity and durability for both AOPs and water splitting. In addition, accelerated dye degradation was observed under water splitting conditions, further highlighting the cooperative effect between the two processes. When configured as both anode and cathode in an anion-exchange-membrane electrolyzer operating in reclaimed water, the medium-entropy metallic glass electrodes sustained a current density of 200 mA cm^{-2} at approximately 1.96 V for more than 100 h, with only a moderate increase in cell voltage over time. Although challenges associated with electrolyzer corrosion in reclaimed water remain, the low cost and high catalytic performance of this bifunctional system underscore the feasibility of water electrolysis in reclaimed water and highlight its potential for industrial applications.

Acknowledgements This work was supported by the National Natural Science Foundation of China (Grant No. 52271028), the Key Research and Development Program of Heilongjiang Province (2024ZX02C24), and Hongxian Shen gratefully acknowledges the support from the National Natural Science Foundation of China (Grant No. 52571184).

Author Contributions Y.F.C., Y.H.W., and S.D.J. designed this project and the experiment. Y.F.C., B.L., H.Q.L., and Y.H.W. conducted the experiments. Y.F.C and L.B. prepared the fibers. Y.F.C and J.Q.H. performed conducted the AEM tests. Y.F.C and S.D.J. co-wrote the paper. M. K. M., M. S., S.F. G., H.X.S., J.F.S., and S.D.J. reviewed the paper. The results and manuscript are commented and discussed by all authors.

Declarations

Conflict of interest The authors declare no interest conflict. They have no known competing financial interests or personal relationships that could have appeared to influence the work reported in this paper.

Supplementary Information The online version contains supplementary material available at https://doi.org/10.1007/s40820-026-02172-1.

References

1. Q. Fu, L.W. Wong, F. Zheng, X. Zheng, C.S. Tsang et al., Unraveling and leveraging *in situ* surface amorphization for enhanced hydrogen evolution reaction in alkaline media. Nat. Commun. **14**, 6462 (2023). https://doi.org/10.1038/s41467-023-42221-6
2. J. Huang, R. Wang, H. Sheng, X. Zhu, R.D. Ross et al., Isotope-dependent Tafel analysis probes proton transfer kinetics during electrocatalytic water splitting. Nat. Chem. (2025). https://doi.org/10.1038/s41557-025-01934-5
3. Z. Li, R. Wu, D. Duan, X. Liu, R. Li et al., Empowering multicomponent alloys with unique nanostructure for exceptional oxygen evolution performance through self-replenishment. Joule **8**(10), 2920–2937 (2024). https://doi.org/10.1016/j.joule.2024.06.023
4. L. Tao, K. Wang, F. Lv, H. Mi, F. Lin et al., Precise synthetic control of exclusive ligand effect boosts oxygen reduction catalysis. Nat. Commun. **14**, 6893 (2023). https://doi.org/10.1038/s41467-023-42514-w
5. H. Yu, Y. Ji, C. Li, W. Zhu, Y. Wang et al., Strain-triggered distinct oxygen evolution reaction pathway in two-dimensional metastable phase IrO_2 *via* CeO_2 loading. J. Am. Chem. Soc. **146**(29), 20251–20262 (2024). https://doi.org/10.1021/jacs.4c05204
6. F. Lyu, S. Zeng, Z. Jia, F.-X. Ma, L. Sun et al., Two-dimensional mineral hydrogel-derived single atoms-anchored heterostructures for ultrastable hydrogen evolution. Nat. Commun. **13**, 6249 (2022). https://doi.org/10.1038/s41467-022-33725-8
7. S. Jiao, X. Fu, S. Wang, Y. Zhao, Perfecting electrocatalysts *via* imperfections: towards the large-scale deployment of water electrolysis technology. Energy Environ. Sci. **14**(4), 1722–1770 (2021). https://doi.org/10.1039/D0EE03635H
8. L. Hou, Z. Li, H. Jang, Y. Wang, X. Cui et al., Electronic and lattice engineering of ruthenium oxide towards highly

active and stable water splitting. Adv. Energy Mater. **13**(22), 2300177 (2023). https://doi.org/10.1002/aenm.202300177

9. Y. Zhou, H. Liu, X. Gu, X. Wu, L. Feng, Hetero MOF-on-MOF-derived carbon nanotube interconnected nitrogen-doped carbon-encapsulated FeNi/FeF_2 for efficient oxygen evolution reaction. Carbon Energy **4**(5), 924–938 (2022). https://doi.org/10.1002/cey2.206
10. X. Gu, Z. Liu, M. Li, J. Tian, L. Feng, Surface structure regulation and evaluation of FeNi-based nanoparticles for oxygen evolution reaction. Appl. Catal. B Environ. **297**, 120462 (2021). https://doi.org/10.1016/j.apcatb.2021.120462
11. Y. Fang, Y. Hou, X. Fu, X. Wang, Semiconducting polymers for oxygen evolution reaction under light illumination. Chem. Rev. **122**(3), 4204–4256 (2022). https://doi.org/10.1021/acs.chemrev.1c00686
12. Y. Fang, Y. Xu, X. Li, Y. Ma, X. Wang, Coating polymeric carbon nitride photoanodes on conductive Y: ZnO nanorod arrays for overall water splitting. Angew. Chem. **130**(31), 9897–9901 (2018). https://doi.org/10.1002/ange.201804530
13. L. Li, G. Zhang, C. Zhou, F. Lv, Y. Tan et al., Lanthanide-regulating Ru-O covalency optimizes acidic oxygen evolution electrocatalysis. Nat. Commun. **15**, 4974 (2024). https://doi.org/10.1038/s41467-024-49281-2
14. J. Xie, F. Wang, Y. Zhou, Y. Dong, Y. Chai et al., Internal polarization field induced hydroxyl spillover effect for industrial water splitting electrolyzers. Nano-Micro Lett. **16**(1), 39 (2023). https://doi.org/10.1007/s40820-023-01253-9
15. Z. Jiang, S. Song, X. Zheng, X. Liang, Z. Li et al., Lattice strain and Schottky junction dual regulation boosts ultrafine ruthenium nanoparticles anchored on a N-modified carbon catalyst for H_2 production. J. Am. Chem. Soc. **144**(42), 19619–19626 (2022). https://doi.org/10.1021/jacs.2c09613
16. M. Wei, Y. Sun, J. Zhang, F. Ai, S. Xi et al., High-entropy alloy nanocrystal assembled by nanosheets with d–d electron interaction for hydrogen evolution reaction. Energy Environ. Sci. **16**(9), 4009–4019 (2023). https://doi.org/10.1039/d3ee01929b
17. K. Li, W. Qiao, N. Li, M. Lü, C. Gu et al., Ultrafast microwave construction of stabilized RuCo alloys for overall water splitting. J. Chem. Phys. **162**(24), 244702 (2025). https://doi.org/10.1063/5.0268895
18. X. Gao, P. Wang, X. Sun, M. Jaroniec, Y. Zheng et al., Membrane-free water electrolysis for hydrogen generation with low cost. Angew. Chem. Int. Ed. **64**(6), e202417987 (2025). https://doi.org/10.1002/anie.202417987
19. Y. Huang, W. Zhou, L. Xie, X. Meng, J. Li et al., Self-sacrificing and self-supporting biomass carbon anode–assisted water electrolysis for low-cost hydrogen production. Proc. Natl. Acad. Sci. U. S. A. **121**(47), e2316352121 (2024). https://doi.org/10.1073/pnas.2316352121
20. Z. He, Y. He, Y. Qiu, Q. Zhao, Z. Wang et al., Monolithic-structured nickel silicide electrocatalyst for bifunctionally efficient overall water splitting. Appl. Catal. B Environ. **342**, 123386 (2024). https://doi.org/10.1016/j.apcatb.2023.123386
21. F. Meharban, C. Lin, X. Wu, L. Tan, H. Wang et al., Scaling up stability: navigating from lab insights to robust oxygen evolution electrocatalysts for industrial water electrolysis. Adv. Energy Mater. **14**(41), 2402886 (2024). https://doi.org/10.1002/aenm.202402886
22. J. Chang, G. Wang, M. Wang, Q. Wang, B. Li et al., Improving Pd–N–C fuel cell electrocatalysts through fluorination-driven rearrangements of local coordination environment. Nat. Energy **6**(12), 1144–1153 (2021). https://doi.org/10.1038/s41560-021-00940-4
23. Y. Sun, H. Liao, J. Wang, B. Chen, S. Sun et al., Covalency competition dominates the water oxidation structure–activity relationship on spinel oxides. Nat. Catal. **3**(7), 554–563 (2020). https://doi.org/10.1038/s41929-020-0465-6
24. L.-L. Wang, X.-R. Wang, H.-J. Wang, C. Zhang, J.-J. Li et al., Tailoring lewis acidity of metal oxides on nickel to boost electrocatalytic hydrogen evolution in neutral electrolyte. J. Am. Chem. Soc. **147**(9), 7555–7563 (2025). https://doi.org/10.1021/jacs.4c16596
25. Q. Guo, R. Li, Y. Zhang, Q. Zhang, Y. He et al., Durable acidic oxygen evolution *via* self-construction of iridium oxide/iridium-tantalum oxide bi-layer nanostructure with dynamic replenishment of active sites. Nano-Micro Lett. **17**(1), 165 (2025). https://doi.org/10.1007/s40820-025-01680-w
26. X. Mao, M. Zhu, M. Xie, G. Zou, Y. Kuang et al., Ultralow-iridium oxygen evolution catalyst with dual-site oxide pathway for proton exchange membrane water electrolysis. Nano Lett. **25**(45), 16253–16261 (2025). https://doi.org/10.1021/acs.nanolett.5c04543
27. J. Kang, X. Qiu, Q. Hu, J. Zhong, X. Gao et al., Valence oscillation and dynamic active sites in monolayer NiCo hydroxides for water oxidation. Nat. Catal. **4**(12), 1050–1058 (2021). https://doi.org/10.1038/s41929-021-00715-w
28. A. Pei, R. Xie, Y. Zhang, Y. Feng, W. Wang et al., Effective electronic tuning of Pt single atoms *via* heterogeneous atomic coordination of (Co, Ni)$(OH)_2$ for efficient hydrogen evolution. Energy Environ. Sci. **16**(3), 1035–1048 (2023). https://doi.org/10.1039/d2ee02785b
29. Y. Zhou, L. Zhao, G. Xu, N. Wang, X. Chen et al., H* site-blocking alleviated through collaborative copper alloying for large-current hydrogen production. Adv. Energy Mater. **15**(35), 2501852 (2025). https://doi.org/10.1002/aenm.202501852
30. L. Yi, S. Xiao, Y. Wei, D. Li, R. Wang et al., Free-standing high-entropy alloy plate for efficient water oxidation catalysis: structure/composition evolution and implication of high-valence metals. Chem. Eng. J. **469**, 144015 (2023). https://doi.org/10.1016/j.cej.2023.144015
31. X. Wang, W. Pi, S. Hu, H. Bao, N. Yao et al., Boosting oxygen evolution reaction performance on NiFe-based catalysts through d-orbital hybridization. Nano-Micro Lett. **17**(1), 11 (2024). https://doi.org/10.1007/s40820-024-01528-9
32. Y. Chen, Q. Li, Y. Lin, J. Liu, J. Pan et al., Boosting oxygen evolution reaction by FeNi hydroxide-organic framework electrocatalyst toward alkaline water electrolyzer. Nat. Commun. **15**, 7278 (2024). https://doi.org/10.1038/s41467-024-51521-4
33. Q. Yu, Y. Chen, J. Liu, C. Li, J. Hu et al., MXene-mediated reconfiguration induces robust nickel–iron catalysts for

industrial-grade water oxidation. Proc. Natl. Acad. Sci. U. S. A. **121**(9), e2319894121 (2024). https://doi.org/10.1073/pnas.2319894121

34. Z. Zhu, Y. Lin, P. Fang, M. Wang, M. Zhu et al., Orderly nanodendritic nickel substitute for raney nickel catalyst improving alkali water electrolyzer. Adv. Mater. **36**, 2307035 (2024). https://doi.org/10.1002/adma.202307035
35. H. Xie, Z. Zhao, T. Liu, Y. Wu, C. Lan et al., A membrane-based seawater electrolyser for hydrogen generation. Nature **612**(7941), 673–678 (2022). https://doi.org/10.1038/s41586-022-05379-5
36. Y. Zhang, W. Wan, Y. Peng, Y. Guo, J. Zhou et al., Corrosion-resistant single-atom catalysts for direct seawater electrolysis. Natl. Sci. Rev. **12**(4), nwaf060 (2025). https://doi.org/10.1093/nsr/nwaf060
37. A. Badreldin, J. Abed, N. Hassan, A. El-Ghenymy, W. Suwaileh et al., Sulfide interlayered cobalt-based oxynitrides for efficient oxygen evolution reaction in neutral pH water and seawater. Appl. Catal. B Environ. **330**, 122599 (2023). https://doi.org/10.1016/j.apcatb.2023.122599
38. J. Li, G. Fu, X. Sheng, G. Li, H. Chen et al., A comprehensive review on catalysts for seawater electrolysis. Adv. Powder Mater. **3**(5), 100227 (2024). https://doi.org/10.1016/j.apmate.2024.100227
39. Z. Yao, Y. Chen, X. Wang, K. Hu, S. Ren et al., High-entropy alloys catalyzing polymeric transformation of water pollutants with remarkably improved electron utilization efficiency. Nat. Commun. **16**, 148 (2025). https://doi.org/10.1038/s41467-024-55627-7
40. W. Ren, Q. Zhang, J. Chen, X. Xiao, X. Duan et al., Catalytic resource recovery for transformation of the wastewater industry. Nat. Water **3**(11), 1228–1242 (2025). https://doi.org/10.1038/s44221-025-00530-8
41. S. Hong, J. Kim, J. Park, S. Im, M.R. Hoffmann et al., Scalable Ir-doped $NiFe_2O_4/TiO_2$ heterojunction anode for decentralized saline wastewater treatment and H_2 production. Nano-Micro Lett. **17**(1), 51 (2024). https://doi.org/10.1007/s40820-024-01542-x
42. H. Wang, Y. Wang, G. Zhang, Z. Zhao, F. Ju, Temporal dynamics and performance association of the *Tetrasphaera*-enriched microbiome for enhanced biological phosphorus removal. Engineering **29**, 168–178 (2023). https://doi.org/10.1016/j.eng.2022.10.016
43. I.A. Saleh, N. Zouari, M.A. Al-Ghouti, Removal of pesticides from water and wastewater: Chemical, physical and biological treatment approaches. Environ. Technol. Innov. **19**, 101026 (2020). https://doi.org/10.1016/j.eti.2020.101026
44. L. Zhao, J. Zhang, J. Ma, PTIO as a redox mediator to enhance organic contaminants oxidation by permanganate. Water Res. **244**, 120500 (2023). https://doi.org/10.1016/j.watres.2023.120500
45. Z. Jia, Q. Wang, L. Sun, Q. Wang, L.-C. Zhang et al., Attractive *in situ* self-reconstructed hierarchical gradient structure of metallic glass for high efficiency and remarkable stability in catalytic performance. Adv. Funct. Mater. **29**(19), 1807857 (2019). https://doi.org/10.1002/adfm.201807857
46. Y. Yang, Z. Jia, Q. Wang, Y. Liu, L. Sun et al., Vacancy induced microstrain in high-entropy alloy film for sustainable hydrogen production under universal pH conditions. Energy Environ. Sci. **17**(16), 5854–5865 (2024). https://doi.org/10.1039/d4ee01139b
47. T. Liu, S. Xiao, N. Li, J. Chen, X. Zhou et al., Water decontamination *via* nonradical process by nanoconfined Fenton-like catalysts. Nat. Commun. **14**, 2881 (2023). https://doi.org/10.1038/s41467-023-38677-1
48. G. Dong, B. Chen, B. Liu, L.J. Hounjet, Y. Cao et al., Advanced oxidation processes in microreactors for water and wastewater treatment: Development, challenges, and opportunities. Water Res. **211**, 118047 (2022). https://doi.org/10.1016/j.watres.2022.118047
49. C. Chen, Y.-R. Wang, Y.-J. Wang, J.-H. Zhou, Y.-Q. Li et al., Built-in electric field augments hypersalinity resistance of heterostructured metal oxides for efficient Fenton-like catalysis. ACS Nano **19**(32), 29616–29626 (2025). https://doi.org/10.1021/acsnano.5c08552
50. Z. Chen, F. An, Y. Zhang, Z. Liang, W. Liu et al., Single-atom Mo–Co catalyst with low biotoxicity for sustainable degradation of high-ionization-potential organic pollutants. Proc. Natl. Acad. Sci. U. S. A. **120**(29), e2305933120 (2023). https://doi.org/10.1073/pnas.2305933120
51. Y. Wen, Y. Zhao, M. Guo, Y. Xu, Synergetic effect of Fe_2O_3 and $BiVO_4$ as photocatalyst nanocomposites for improved photo-Fenton catalytic activity. J. Mater. Sci. **54**(11), 8236–8246 (2019). https://doi.org/10.1007/s10853-019-03511-x
52. L. Wu, W. Lu, W.L. Ong, A.S.W. Wong, Y. Zhang et al., Photothermal-promoted anion exchange membrane seawater electrolysis on a nickel-molybdenum-based catalyst. Nat. Commun. **16**, 3098 (2025). https://doi.org/10.1038/s41467-025-58320-5
53. R. Lu, B. Wang, L. Li, Z. Bao, B. Li et al., Advances in direct seawater electrolysis for green hydrogen production: emerging technologies and future perspectives. Sci. Bull. **71**(1), 172–195 (2026). https://doi.org/10.1016/j.scib.2025.09.032
54. T. Liu, C. Lan, M. Tang, M. Li, Y. Xu et al., Redox-mediated decoupled seawater direct splitting for H_2 production. Nat. Commun. **15**, 8874 (2024). https://doi.org/10.1038/s41467-024-53335-w
55. W. Chao, X. Yan, L. Lu, High spatiotemporal availability of hydrogen by electrolysis of municipal reclaimed water in China. Environ. Sci. Technol. **59**(31), 16344–16355 (2025). https://doi.org/10.1021/acs.est.5c01203
56. H.B. Tao, Y. Xu, X. Huang, J. Chen, L. Pei et al., A general method to probe oxygen evolution intermediates at operating conditions. Joule **3**(6), 1498–1509 (2019). https://doi.org/10.1016/j.joule.2019.03.012
57. S. Lu, X. Li, G. Zhang, S. Wang, Unlocking single-atom induced electronic metal-support interactions in electrocatalytic one-electron water oxidation for wastewater purification. Nat. Commun. **16**, 4346 (2025). https://doi.org/10.1038/s41467-025-59722-1
58. Y.-J. Zhang, J.-S. Tao, Y. Hu, G.-X. Huang, Y. Pan et al., Metal oxyhalide-based heterogeneous catalytic water purification

 https://doi.org/10.1007/s40820-026-02172-1

with ultralow H_2O_2 consumption. Nat. Water **2**(8), 770–781 (2024). https://doi.org/10.1038/s44221-024-00281-y

59. C. Kim, S. Kim, Y. Park, W. Choi, Bifunctional Fenton-like catalyst enabling oxidative and reductive removal of contaminants synergically in chemical reagent-free aerated solution. Appl. Catal. B Environ. **341**, 123287 (2024). https://doi.org/10.1016/j.apcatb.2023.123287
60. M. Liu, S. Ning, D. Xiao, Y. Zhang, J. Han et al., Amorphous/crystalline heterostructured nanoporous high-entropy metallic glasses for efficient water splitting. Mater. Futures **4**(2), 025303 (2025). https://doi.org/10.1088/2752-5724/add415
61. L. Liu, L. Shao, Y. Ma, Z. Wen, J. Zhou et al., Sparse nanocrystals enable ultra-low coercivity and remarkable mechanical robustness in high-entropy amorphous alloy. Adv. Sci. **12**(38), e03546 (2025). https://doi.org/10.1002/advs.202503546
62. G. Wang, Z. Chen, J. Zhu, J. Xie, W. Wei et al., High-entropy amorphous catalysts for water electrolysis: a new frontier. Nano-Micro Lett. **18**(1), 77 (2025). https://doi.org/10.1007/s40820-025-01936-5
63. S.-Q. Yue, T. Liu, F.-Y. Kong, D.-H. Wen, W.-L. Song et al., Breaking the paradox between glass-forming and α-Fe nanocrystallizing abilities in Fe-based alloys. Rare Met. **44**(10), 7876–7888 (2025). https://doi.org/10.1007/s12598-025-03410-y
64. Z.-J. Guo, Y.-S. Luo, M.-Q. Xu, M.-T. Xue, B.-Y. Cai et al., Biomedical Ti–Zr–Mo–Cu medium-entropy alloys with excellent mechanical and antibacterial properties by various quenching processes. Rare Met. **44**(11), 9144–9158 (2025). https://doi.org/10.1007/s12598-025-03582-7
65. B. Li, S.-D. Jiang, Q. Fu, R. Wang, W.-Z. Xu et al., Tailoring nanocrystalline/amorphous interfaces to enhance oxygen evolution reaction performance for FeNi-based alloy fibers. Adv. Funct. Mater. **35**(2), 2413088 (2025). https://doi.org/10.1002/adfm.202413088
66. S.-D. Jiang, T. Eggers, O. Thiabgoh, C. Wang, J.-T. Huo et al., Design of core-shell structured magnetic microwire with desirable properties for multifunctional applications. Small **21**(23), 2500455 (2025). https://doi.org/10.1002/smll.202500455
67. S. Jiang, H. Wang, D. Estevez, Y. Huang, L. Zhang et al., Surface microstructural design to improve mechanical and giant magneto-impedance properties of melt-extracted CoFe-based amorphous wires. Mater. Des. **204**, 109642 (2021). https://doi.org/10.1016/j.matdes.2021.109642
68. H. Wang, F.X. Qin, D.W. Xing, F.Y. Cao, X.D. Wang et al., Relating residual stress and microstructure to mechanical and giant magneto-impedance properties in cold-drawn co-based amorphous microwires. Acta Mater. **60**(15), 5425–5436 (2012). https://doi.org/10.1016/j.actamat.2012.06.047
69. J.C. Wang, Z. Jia, S.X. Liang, P. Qin, W.C. Zhang et al., $Fe_{73.5}Si_{13.5}B_9Cu_1Nb3$ metallic glass: rapid activation of peroxymonosulfate towards ultrafast *Eos* in Y degradation. Mater. Des. **140**, 73–84 (2018). https://doi.org/10.1016/j.matdes.2017.11.049
70. D. Xing, H. Shen, S. Jiang, J. Liu, M.-H. Phan et al., Magnetocaloric effect and critical behavior in melt-extracted $Gd_{60}Co_{15}Al_{25}$microwires: magnetocaloric effect and critical behavior in $Gd_{60}Co_{15}Al_{25}$microwires. Phys. Status Solidi A **212**(9), 1905–1910 (2015). https://doi.org/10.1002/pssa.201532192
71. J. Liu, Z. Du, S. Jiang, H. Shen, Z. Li et al., Tailoring giant magnetoimpedance effect of co-based microwires for optimum efficiency by self-designed square-wave pulse current annealing. J. Magn. Magn. Mater. **385**, 145–150 (2015). https://doi.org/10.1016/j.jmmm.2015.02.050
72. H. Shen, L. Luo, Y. Bao, H. Yin, S. Jiang et al., New DyHoCo medium entropy amorphous microwires of large magnetic entropy change. J. Alloys Compd. **837**, 155431 (2020). https://doi.org/10.1016/j.jallcom.2020.155431
73. H. Yin, Y. Huang, Y. Bao, S. Jiang, P. Xue et al., Comparable magnetocaloric properties of melt-extracted $Gd_{36}Tb_{20}Co_{20}Al_{24}$ metallic glass microwires. J. Alloys Compd. **815**, 150983 (2020). https://doi.org/10.1016/j.jallcom.2019.06.085
74. Q. Zhang, S.-X. Liang, Z. Jia, W. Zhang, W. Wang et al., Efficient nanostructured heterogeneous catalysts by electrochemical etching of partially crystallized Fe-based metallic glass ribbons. J. Mater. Sci. Technol. **61**, 159–168 (2021). https://doi.org/10.1016/j.jmst.2020.06.016
75. S. Pei, S. Wang, Y. Lu, X. Li, B. Wang, Application of metal-based catalysts for Fenton reaction: from homogeneous to heterogeneous, from nanocrystals to single atom. Nano Res. **17**(11), 9446–9471 (2024). https://doi.org/10.1007/s12274-024-6973-y
76. X. Zhang, J. Wei, C. Wang, L. Wang, Z. Guo et al., Recent advance of Fe-based bimetallic persulfate activation catalysts for antibiotics removal: performance, mechanism, contribution of the key ROSs and degradation pathways. Chem. Eng. J. **487**, 150514 (2024). https://doi.org/10.1016/j.cej.2024.150514
77. C. Zhang, Q. Sun, K. Liu, From adsorption to reductive degradation: different decolorization properties of metallic glasses based on different iron-group elements. J. Alloys Compd. **741**, 1040–1047 (2018). https://doi.org/10.1016/j.jallcom.2018.01.213
78. C. Zhang, N. Ding, Y. Pan, L. Fu, Y. Zhang, The degradation pathways of contaminants by reactive oxygen species generated in the Fenton/Fenton-like systems. Chin. Chem. Lett. **35**(10), 109579 (2024). https://doi.org/10.1016/j.cclet.2024.109579
79. Y.-H. Wang, B. Li, Y.-F. Cui, Y. Du, Z.-W. Yu et al., Catalytic mechanism of nanocrystalline and amorphous matrix in Fe-based microwires for advanced oxidation. Adv. Funct. Mater. **35**(29), 2425912 (2025). https://doi.org/10.1002/adfm.202425912
80. D. Lai, Q. Kang, F. Gao, Q. Lu, High-entropy effect of a metal phosphide on enhanced overall water splitting performance. J. Mater. Chem. A **9**(33), 17913–17922 (2021). https://doi.org/10.1039/d1ta04755h
81. X. Zhao, H. Zhang, Y. Yan, J. Cao, X. Li et al., Engineering the electrical conductivity of lamellar silver-doped cobalt(II) selenide nanobelts for enhanced oxygen evolution. Angew. Chem. **129**(1), 334–338 (2017). https://doi.org/10.1002/ange.201609080

82. M.G. Walter, E.L. Warren, J.R. McKone, S.W. Boettcher, Q. Mi et al., Solar water splitting cells. Chem. Rev. **110**(11), 6446–6473 (2010). https://doi.org/10.1021/cr1002326
83. Y.-F. Cui, S.-D. Jiang, Q. Fu, R. Wang, P. Xu et al., Cost-effective high entropy core–shell fiber for stable oxygen evolution reaction at 2 A cm^{-2}. Adv. Funct. Mater. **33**(50), 2306889 (2023). https://doi.org/10.1002/adfm.202306889
84. M. Zuo, S. Yi, J. Choi, Excellent dye degradation performance of FeSiBP amorphous alloys by Fenton-like process. J. Environ. Sci. **105**, 116–127 (2021). https://doi.org/10.1016/j.jes.2020.12.032
85. J. Su, Y. Yang, G. Xia, J. Chen, P. Jiang et al., Ruthenium-cobalt nanoalloys encapsulated in nitrogen-doped graphene as active electrocatalysts for producing hydrogen in alkaline media. Nat. Commun. **8**, 14969 (2017). https://doi.org/10.1038/ncomms14969
86. Y. Li, Y. Wu, M. Yuan, H. Hao, Z. Lv et al., Operando spectroscopies unveil interfacial FeOOH induced highly reactive β-Ni(Fe)OOH for efficient oxygen evolution. Appl. Catal. B Environ. **318**, 121825 (2022). https://doi.org/10.1016/j.apcatb.2022.121825
87. X. Chen, X. Xu, Y. Cheng, H. Liu, D. Li et al., Achieving high-performance electrocatalytic water oxidation on $Ni(OH)_2$ with optimized intermediate binding energy enabled by S-doping and CeO_2-interfacing. Small **20**(8), 2303169 (2024). https://doi.org/10.1002/smll.202303169
88. A. Gao, S. Shen, T. Shang, Y. Shi, H. Zhang et al., Van der Waals phase transition investigation toward high-voltage layered cathodes. Sci. Adv. **10**(33), eadp4906 (2024). https://doi.org/10.1126/sciadv.adp4906
89. S. Shen, Z. Wang, Z. Lin, K. Song, Q. Zhang et al., Crystalline-amorphous interfaces coupling of $CoSe_2$/CoP with optimized d-band center and boosted electrocatalytic hydrogen evolution. Adv. Mater. **34**(13), 2110631 (2022). https://doi.org/10.1002/adma.202110631
90. T. Tang, J. Han, Z. Wang, X. Niu, J. Guan, Diatomic Fe-Co catalysts synergistically catalyze oxygen evolution reaction. Nano Res. **17**(5), 3794–3800 (2024). https://doi.org/10.1007/s12274-023-6318-2

 https://doi.org/10.1007/s40820-026-02172-1